

# Anthropogenic Influence on Long-Term Surface Air Temperature Trends: Attribution of Temperature Changes Across East Asia

S. Allabakash

Korea Institute of Civil Engineering and Building Technology

S. Lim (✉ [slim@kict.re.kr](mailto:slim@kict.re.kr))

Korea Institute of Civil Engineering and Building Technology <https://orcid.org/0000-0002-0545-9369>

---

## Research Article

**Keywords:** Climate change, Detection and attribution, CMIP6, East Asia, Future projections

**Posted Date:** July 8th, 2021

**DOI:** <https://doi.org/10.21203/rs.3.rs-207433/v2>

**License:**   This work is licensed under a Creative Commons Attribution 4.0 International License.

[Read Full License](#)

---

1 **Anthropogenic influence on long-term surface air temperature trends:**

2 **Attribution of temperature changes across East Asia**

3  
4 S. Allabakash and S. Lim\*

5 Korea Institute of Civil Engineering and Building Technology, Ilsan, Goyang, South Korea

6

7

8

9

10

11

12

13

14

15

16

17

18

19

20 \*Corresponding author: S. Lim; 283, Korea Institute of Civil Engineering and Building Technology, Goyang-daero,

21 Ilsanseo-gu, Goyang-si, Gyeonggi-do 10223, South Korea, (slim@kict.re.kr).

22

23  
24  
25  
26  
27  
28  
29  
30  
31  
32  
33  
34  
35  
36  
37  
38  
39  
40  
41  
42

## ABSTRACT

Climate change is an ongoing process impacting ecosystem functions and human health; East Asia (EA) is one of the most vulnerable regions being influenced by such changes. This study examines the long-term variability of surface air temperatures (SATs) across EA using the new Coupled Model Intercomparison Project Phase 6 (CMIP6) datasets. Historical simulations (20<sup>th</sup> century) and future (21<sup>st</sup> century) SAT projections were investigated based on multi-model ensemble simulations. We also demonstrate the contribution of external and natural (NAT) forcings to SAT change. This study mainly focuses the effect of anthropogenic forcings (ANT) on EA climate for a long period (1850-2100). Our simulations show that SAT in EA increased by 0.031 °C/decade during the period 1850–2014 owing to combined ANT and NAT (‘ALL=ANT+NAT’) forcings, while an increase of 0.08 °C/decade can be attributed to greenhouse gas (GHG) emissions. The ANT forcing rapidly increased after the third industrial revolution (after 1969). Consequently, SAT change accelerated to 0.255 °C/decade and 0.268 °C/decade owing to ALL and GHG forcings, respectively. Human-induced GHG emissions and land use were the dominant factors driving SAT warming during the study period, and will contribute to substantial future warming trends. Furthermore, optimal fingerprinting method demonstrates the significance of ANT influences on climate change in EA. ANT forcing was clearly detected and distinct from NAT forcing in a two-signal analysis. In a three-signal analysis, GHG was clearly detected for EA region in separation from ANT and NAT influences. The shared socioeconomic pathway emission scenarios (SSP1–2.6, SSP2–4.5, and SSP5–8.5) showed future projections (warming trends) from 2015–2100. This analysis suggests that climate change could be mitigated by restricting anthropogenic factors (especially GHG) and land use/activities in EA.

Keywords: Climate change, Detection and attribution, CMIP6, East Asia, Future projections

## 43 1. Introduction

44 The world faces the major challenge of on-going climate change, which greatly impacts socioeconomic and  
45 human activities as well as human health (IPCC 2013; Stocker et al. 2014). For example, during the 20<sup>th</sup> century,  
46 average surface air temperatures (SATs) have increased by 0.6 °C worldwide (IPCC 2013; Stocker et al. 2014). Many  
47 authors have investigated the effects of external forcing on mean temperatures at global and regional scales, with  
48 increases primarily attributed to anthropogenic greenhouse gas (GHG) emissions alongside other human forcings  
49 (Stott et al. 2010; Bindoff et al. 2013; Jones et al. 2013). Meehl et al. (2004) explored a combination of natural and  
50 anthropogenic forcing using a parallel climate model, finding that natural (solar) forcing dominated warming during  
51 the early 20<sup>th</sup> century and anthropogenic forcing (GHG emissions) dominated the late 21<sup>st</sup>-century warming. Egorova  
52 et al. (2018) also reported an annual mean global warming rate of 0.3 K during the early 20<sup>th</sup> century (1910–1940),  
53 with approximately half of this warming attributed to CO<sub>2</sub>, CH<sub>4</sub>, and N<sub>2</sub>O (well-mixed GHGs), and approximately  
54 one-third attributed to solar irradiance.

55 East Asia (EA) is one of the regions most vulnerable to climate change. It is one of the most densely populated  
56 regions, containing several major industrial and agricultural centers including high-altitude areas such as the Tibetan  
57 Plateau. Thus, the EA region is sensitive to climate change that impacts the global climate as well. Therefore,  
58 understanding and assessing climate change across EA is important for estimating and predicting global climate  
59 change (Zhou et al. 2004). Increasing SAT trends in EA have been linked to extreme weather events (Xuejie et al.  
60 2002; Li et al. 2018) including heatwaves (Yoon et al. 2018) and intense precipitation (Paik et al. 2020). In response  
61 to these challenges, many studies have described the characteristics of SAT changes in EA countries. In China, Tang  
62 et al. (2010) reported that SAT increased by  $0.78 \pm 0.27$  °C between 1906 and 2005, and Xu et al. (2015) observed a  
63 warming of 0.25 °C/decade and 0.17 °C/decade between 1961 and 2005 as a result of GHG emissions and other  
64 anthropogenic factors, respectively. The same authors reported that the emission of GHGs is the dominant factor  
65 forcing impacting climate change in China. Qian and Qin (2006) analyzed the spatiotemporal characteristics of  
66 temperature trends across China using data from 486 meteorological stations, reporting increases of 0.2–0.3 °C/decade  
67 and < 0.1 °C/decade in northern and southern China, respectively, between 1960 and 2000. The same authors report  
68 that the greatest increases occurred in winter temperatures (0.5–0.7 °C/decade and 0.2–0.3 °C/decade in northern and  
69 southern China, respectively). Mean annual temperature changes in China between 1961 and 2005 were attributed to

70 the combined effect of GHG emissions and sulfate aerosol forcing (Xu et al. 2015). Across the Korean Peninsula,  
71 extreme heatwave events have also been associated with climate change (Yoon et al. 2020). In North Korea, Om et al.  
72 (2019) observed a temperature change of 0.21 °C/decade from 1918 to 2015, which is higher than the changes reported  
73 for mainland China and the global average. Coastal areas were found to experience lower warming trends than inland  
74 regions in North Korea. Similarly, Jung et al. (2002) observed that mean annual SATs in South Korea increased at a  
75 rate of 0.23 °C/decade between 1954 and 1999, with a higher warming rate during winter. Across the entire Korean  
76 Peninsula, Chung and Yoon (2000) reported that the annual mean temperature increased by 0.42 °C/decade between  
77 1974 and 1997 in association with GHG emissions, with larger cities experiencing faster warming trends than rural  
78 areas and small cities. Wang et al. (2016) also reported a 0.35 °C/decade warming in northeast China and a  
79 0.2 °C/decade warming in Hokkaido, Japan, between 1951 and 2000. They also observed that extreme high- and low-  
80 temperature events were significantly positively correlated between these two regions and the warming recorded in  
81 these regions was in the context of global change. Moreover, in Japan, Fujibe (2009) observed that SATs in regions  
82 with population densities of over 100 and 3,000 persons km<sup>-2</sup> increased at a rate of 0.03–0.05 °C/decade and  
83 0.1 °C/decade, respectively, between 1979 and 2006.

84         Detection and attribution analysis is a versatile tool that can be used to identify the drivers of climate change  
85 (Allen and Tett 1999; Allen and Stott 2003; Ribes and Terray 2013; Ribes et al. 2013; Wang et al. 2018). Several  
86 researchers have used this method to examine temperature increases from regional to global scales, with anthropogenic  
87 forcing being identified as the dominant factor in most cases (e.g., Lu et al. 2016; Weller et al. 2016; Wang et al. 2018;  
88 Paik and Min 2020). Detection and attribution analyses have been performed using the Coupled Model  
89 Intercomparison Project Phase 3 (CMIP3; Santer et al. 2009), Phase 5 (CMIP5; Xu et al. 2015; Yin et al. 2017; Zhang  
90 et al. 2019), and the new Phase 6 (CMIP6) model simulations (Paik and Min 2020; Paik et al. 2020) to assess the  
91 relative contributions of various external forcings to climate change. Xu et al. (2015) used an optimal detection  
92 technique to identify distinct GHG- and anthropogenic (ANT)-associated temperature changes in China between 1961  
93 and 2005; Yin et al. (2017) used multimodal CMIP5 simulations for the period 1958–2012 to detect ANT forcing of  
94 both extreme cold and warm temperatures in China; and Paik et al. (2020) reported that anthropogenic GHG emissions  
95 are the major contributor to extreme precipitation events across a range of climatic settings. As an attribution technique,  
96 the optimal fingerprinting method detects both anthropogenic and natural forcings (referred to as ‘ALL’ forcing) and  
97 ANT forcing (Allen and Tett 1999, Ribes and Terray 2013). Applying this approach to China, Wang et al. (2018)

98 showed that warming in western China can be attributed to anthropogenic forcing, and also projected the future  
99 warming trends of this region. Yin et al. (2017) detected human influences on the intensity of extreme temperature  
100 changes in China, as well as at regional scales in eastern and western China, from 1958–2012. Lu et al. (2016) found  
101 anthropogenic influences on the frequency of daily temperature extremes in China using detection and attribution  
102 analysis. Furthermore, model-simulated responses were consistent with observations of the daytime extremes. Many  
103 researchers have described anthropogenic influences on changes in temperature and precipitation over China (Song et  
104 al. 2015; Burke et al. 2016; Sun et al. 2016; Li et al. 2017; Ma et al. 2017; Li et al. 2018a; Qian et al. 2018; Zeng et  
105 al. 2019).

106 Most of the studies mentioned above focused on climate change in China and few studies have focused on  
107 Korea or Japan. Furthermore, most studies have considered the period 1950–2010 and employed CMIP3 and CMIP5  
108 model simulations. To the best of our knowledge, CMIP6 datasets have not yet been used to examine EA climate  
109 trends during the historical period from 1850 to 2014 nor have future projections (2015–2100) been provided at this  
110 scale. There are also no detection and attribution studies of climate change across the whole of EA. To address this  
111 gap, here we focus on SAT changes in EA between the second half of the 19<sup>th</sup> century and the 21<sup>st</sup> century based on  
112 the new state-of-the-art multi-model CMIP6 simulations. This allows us to describe the contributions of external and  
113 natural forcings on climate change in this region. Based on our analysis, we also describe the relative contributions of  
114 each forcing in each EA country as well as across the EA as a whole. The main focus of the study is to examine the  
115 effect of human-induced/anthropogenic forcings on climate change over EA using CMIP6 simulations. We also  
116 provide future projections of each EA country and the entire EA region based on three different scenarios.

117 The rest of the paper is structured as follows. Section 2 describes the data and methodology and Section 3  
118 provides a discussion of our results including observed and simulated temperature trends in response to the different  
119 forcing factors, the detection and attribution results, and the observation-constrained future projections. Finally, a  
120 summary of our findings and our conclusions are presented in Section 4.

## 121 **2. Data and methodology**

122 We used the CRU time series version 4.03 (resolution =  $0.5^\circ \times 0.5^\circ$ ) and HadCRUT4 (resolution =  $5^\circ \times 5^\circ$ )  
123 observational datasets for the period 1901–2018 and 1850–2019, respectively; the HadCRUT4 dataset (available at  
124 <https://crudata.uea.ac.uk/cru/data/temperature/>) was primarily used to cover the period not considered by the CRU

125 dataset (1850–1900). The CRU data are derived from the interpolation of monthly climate anomalies of worldwide  
126 weather station observations (Peng et al. 2018; Harris et al. 2020; Drumond et al. 2021) and are available at  
127 <https://crudata.uea.ac.uk/cru/data/hrg/>. These CRU data have been used by many researchers studying long-term  
128 temperature and precipitation changes over the EA region (Li et al. 2018b; Peng et al. 2018; Chen et al. 2019; Harris  
129 et al. 2020) and they correlate well with ground station datasets. We separated the land and ocean data, and the former  
130 was used for this study. The state-of-the-art global multimodal simulations of CMIP6 (Eyring et al. 2016), supported  
131 by the World Climate Research Program, were used to estimate the influence of different external forcings and is  
132 available at <https://esgf-node.llnl.gov/projects/cmip6/>. Some of the CMIP6 models are more biased when compared  
133 to observational datasets (Almazroui et al. 2020, Almazroui et al. 2021). Therefore, we used multimodal ensemble  
134 mean values to mitigate any bias and obtain the most accurate values possible. The various CMIP6 models (Table 1)  
135 were re-gridded using bilinear interpolation to achieve a uniform resolution of  $1^\circ \times 1^\circ$ . The 20<sup>th</sup> century historical and  
136 21<sup>st</sup> century future shared socioeconomic pathway (SSP) scenarios were used to define historical and future  
137 temperature trends, respectively. The CMIP6 simulations of historical (ALL), hist-aer (AER), hist-nat (NAT), hist-  
138 GHG (GHG), hist-sol (SOL), and land-hist (LU), which were represent all, anthropogenic aerosol only, natural only,  
139 GHG only, solar irradiance only, and land use only forcings, respectively; and were used to define their influence on  
140 the temperature trends. Robust regression technique was used for the trends estimation, which detect the effects of  
141 outliers and end points (Street et al. 1988). The low SSP1–2.6 and SSP2–4.5 scenarios and high SSP5–8.5 scenarios  
142 were used for the future projections (2015–2100). Initially, the monthly anomalies of the historical (considered land  
143 data and discarded ocean data) datasets (ALL, AER, NAT, GHG, SOL, and LU) and future scenarios (SSP1–2.6,  
144 SSP2–4.5, and SSP5–8.5) were collected from CMIP6. The simulations driven with ALL from 21 models, had 91  
145 runs. The simulations driven by the other forcings of AER, NAT, GHG, LU, and SOL included 10 (46), 10 (48), 11  
146 (46), 8 (13), and 4 (22) models (runs), respectively. Similarly, the future projections driven by SSP1–2.6, SSP2–4.5,  
147 and SSP5–8.5 included 17 (54), 18 (67), and 17 (59) models (runs), respectively (see Table 1). The  $1^\circ \times 1^\circ$  gridded  
148 data were averaged for their respective models. Then, if the grids did not contain any observations, the corresponding  
149 grids of the models were masked out to match the observations. Initially, we averaged all the ensemble members (runs)  
150 for each model, and the multi-model ensemble (MME) mean was estimated as the equally weighted arithmetic average  
151 of all the individual model ensemble means. Monthly anomalies were computed for each grid ( $1^\circ \times 1^\circ$ ) and then yearly  
152 and decadal anomalies were evaluated. Finally, regional mean series were estimated based on the available grid values,

153 weighted by the cosine of the latitude at the center of each grid box area, for each EA country, as well as the entire  
154 EA region.

155 Regularized optimal fingerprinting (ROF) was used for detection and attribution analysis based on the  
156 different forcings (Ribes et al. 2013). This approach can assess the contribution of external forcings based on the  
157 scaling factors in a linear regression model (Allen and Tett 1999; Ribes et al. 2013). ROF is similar to classical optimal  
158 fingerprinting except that a regularized covariance matrix is used for the optimization and estimation of the null-  
159 distribution used for the residual consistency test. ROF is based on the space-time evolution of SAT trends and is  
160 more accurate than the classical optimal detection method (Ribes et al. 2013; Zhang et al. 2019), overcoming the  
161 limitation of empirical orthogonal function truncations. This method generates a full-rank measure of the covariance  
162 matrix of internal variability, which does not require empirical orthogonal function truncation (Ribes et al 2013;  
163 Tokarska et al. 2019). Furthermore, it assumes that the climate response and noise signals are linearly additive, which  
164 means that the observed changes are the sum of climate response (externally forced change) and internally generated  
165 noise (Bindoff et al. 2013; Zhang et al. 2019). In ROF, the observations ( $Y$ ) are regressed onto the MME mean signal  
166 patterns ( $X$ ) using total least squares method (Ribes et al. 2013), such that  $Y = (X - v) \beta + \epsilon$ . Here,  $\beta$  represents an  
167 unknown regression coefficient or scaling factor. All traces of internal variability are not removed from the MME  
168 mean and, therefore, the remaining internal variability effects in  $X$  are represented as  $v$ .  $\epsilon$  is the noise owing to internal  
169 variability (the regression residual). The internal variability ( $\epsilon$ ) was estimated from the model simulations. We used  
170 pre-industrial control (CTL) simulations of 21 models (see Table 1) to estimate internal climate variability and increase  
171 the independent noise data; this reduces the sampling uncertainty in covariance estimations (Ribes et al. 2013). These  
172 CTL simulations were divided into 283 non-overlapping segments that were each 110 years long (the segment length  
173 was equal to the 1905–2014 period used for the detection analysis). The CTL simulations were divided into two sets  
174 of equal size, one was used for optimization and to derive the best estimates, and the other was used to calculate the  
175 5–95% confidence intervals of the scaling factors and also to carry out the residual consistency test (Allen and Tett  
176 1999; Ribes et al. 2013). The residual consistency test uses a nonparametric estimation of the null distribution through  
177 Monte-Carlo simulations to determine whether the noise estimate ( $\epsilon$ ) is consistent with the simulated internal  
178 variability (Ribes and Terray 2013; Tokarska et al. 2019). The influence of the different forcings were detected based  
179 on  $\beta$ . A 90% confidence interval of  $\beta$  greater than zero implies that a corresponding influence of external forcing has  
180 been detected. If the 90% range of  $\beta$  is above zero and it includes unity, this indicates that the observed change is

181 consistent with the model simulations. If the 90% interval of  $\beta$  is greater (less) than unity, this implies that the observed  
 182 changes are underestimated (overestimated) by the model simulations. For further details regarding the ROF method,  
 183 refer to Ribes et al. (2013) and Ribes and Terray (2013).

184 For detection and attribution, we used the MME means of the available simulations for ALL, GHG, ANT,  
 185 and NAT, which largely smoothed the uncorrelated internal variations (Zhang et al. 2019). ANT was estimated by  
 186 subtracting NAT from ALL ( $ANT = ALL - NAT$ ). We conducted one-signal, two-signal, and three-signal analyses  
 187 over the last hundred years (1905–2014) for each EA country and EA overall. Detection and attribution are most  
 188 effective at small data dimensions, allowing better estimation of climate response and, thus, are usually conducted  
 189 within shorter dimensions (Xu et al. 2015). Therefore, we converted the annual data sets into non-overlapping ten-  
 190 year means for the 1905–2014 period, which produced 11 data values (1905–1914, 1915–1924, 1925–1934, ... and  
 191 2005–2014). The use of 10-year temporal means reduced the time dimension, as well as the variability of the  
 192 observations and noise in the climate signals (Wang et al. 2018; Zhang et al. 2019). In the one-signal analysis (Eq. 1),  
 193 the observations were regressed onto MME mean responses of ALL and ANT fingerprints separately to detect their  
 194 relative influence on the observed change. In the two-signal analysis (Eq. 2), the observations were regressed  
 195 simultaneously onto the MME mean responses of ANT and NAT fingerprints to determine their separate contributions.  
 196 In the three-signal analysis (Eq. 4), the observations were regressed onto the MME mean response patterns from the  
 197 GHG, ANTnoGHG (i.e.,  $ANT - GHG$ ), and NAT simulations simultaneously to clearly detect and isolate the GHG  
 198 forcing effect.

$$199 \quad Y_{OBS} = \beta_M X_M + \varepsilon \quad (1)$$

$$200 \quad Y_{OBS} = \beta_{ANT} X_{ANT} + \beta_{NAT} X_{NAT} + \varepsilon \quad (2)$$

$$201 \quad X_{ALL} = X_{ANT} + X_{NAT} \quad (3)$$

$$202 \quad Y_{OBS} = \beta_{GHG} X_{GHG} + \beta_{ANTnoGHG} X_{ANTnoGHG} + \beta_{NAT} X_{NAT} + \varepsilon \quad (4)$$

$$203 \quad X_{ALL} = X_{GHG} + X_{ANTnoGHG} + X_{NAT} \quad (5)$$

204 where  $Y_{OBS}$  represents the observations;  $X$  indicates the model simulations;  $M$  is the fingerprints of ALL, GHG, ANT,  
 205 ANTnoGHG, and NAT;  $\beta$  is the unknown regression coefficient or scaling factor;  $\varepsilon$  is the regression residual term,

206 which represents the noise due to internal variability;  $X_{ALL}$ ,  $X_{GHG}$ ,  $X_{ANT}$ ,  $X_{ANTnoGHG}$ , and  $X_{NAT}$  are the model simulation  
207 responses to the ALL, GHG, ANT, ANTnoGHG, and NAT forcings, respectively; and  $\beta_{GHG}$ ,  $\beta_{ANT}$ ,  $\beta_{ANTnoGHG}$ , and  
208  $\beta_{NAT}$  are scaling factors corresponding to the GHG, ANT, ANTnoGHG, and NAT forcings, respectively.

### 209 3. Results and discussion

#### 210 3.1 Observed and model simulation trends

211 Figures 1a and 1b show the annual mean temperatures from 1901 to 2014 estimated from CRU and CMIP6  
212 (ALL forcings), respectively. The mean temperature varied between  $-15^{\circ}\text{C}$  and  $30^{\circ}\text{C}$  throughout EA. Southeast  
213 China showed the highest mean temperature (approximately  $25^{\circ}\text{C}$ ), while Tibet and northwest Mongolia showed the  
214 lowest ( $< 0^{\circ}\text{C}$ ). In Korea and Japan, the mean temperature varied from  $4$  to  $16^{\circ}\text{C}$ . The performance of the CMIP6  
215 model simulations was validated in comparison with the CRU observations. The bias (CMIP6 – CRU) across EA and  
216 in all EA countries is shown in Figures 1c and 1d. In Figure 1d, the 25% and 75% quartiles indicate a bias of  $< 1.8^{\circ}\text{C}$ .  
217 Overall, the mean bias for EA was  $\leq 0.5^{\circ}\text{C}$ , indicating that the performance of the CMIP6 simulations was satisfactory.  
218 Figures 1a and 1b also show that the mean temperature values of CRU and CMIP6 outputs are consistent. The  
219 Student's t test also showed no significant differences between the observations and model estimations at the selected  
220 time period (significance level  $< 0.05$ ). Further, we compared the trends of the simulations and observations (see  
221 Figure 3 and the following paragraphs), which showed good agreement.

222 We also evaluated the spatial distributions of the annual mean SAT MME mean response trends to the  
223 different forcings for the period 1850–2014. Figures 2a–e correspond to the temperature trends associated with the  
224 ALL, AER, NAT, GHG, and SOL forcings. The trends are estimated based on robust regression analysis. The LU  
225 datasets were only available for very few models and did not cover all the EA regions (Table 1) owing to their low  
226 spatial resolutions. Therefore, the distributions for LU are not presented here. The lowest increases in temperature  
227 owing to ALL and GHG occurred in southeast China, while the highest increases were observed in Tibet and southern  
228 Mongolia. As the third industrial revolution began in 1969, we also estimated the temperature changes over the last  
229 40 years (1971–2014; Table 2). The SAT response to ALL forcings clearly shows a positive trend throughout EA  
230 during the study period, with an increase of approximately  $0.031^{\circ}\text{C}/\text{decade}$  between 1850 and 2014 (Period 1 = P1)  
231 and  $0.255^{\circ}\text{C}/\text{decade}$  between 1971 and 2014 (P2). Overall, Mongolia showed the highest rate of increase at  
232  $0.049^{\circ}\text{C}/\text{decade}$  in P1 and  $0.379^{\circ}\text{C}/\text{decade}$  in P2, and Japan the lowest at  $0.026^{\circ}\text{C}/\text{decade}$  in P1 and  $0.25^{\circ}\text{C}/\text{decade}$

233 in P2. AER showed a negative and the lowest temperature trend in all the EA countries (Figure 2b and Table 2). Thus,  
234 it is determined that AER cools SAT and slows the warming rate. Across EA, the overall AER cooling trend was  
235  $-0.076\text{ }^{\circ}\text{C/decade}$  during P1 and  $-0.035\text{ }^{\circ}\text{C/decade}$  in P2. Interestingly, in P2, Mongolia showed a positive/increasing  
236 trend in association with the highest degree of warming observed in this region. Figure 2c shows that the SAT values  
237 were less influenced by NAT forcing, and Table 2 shows slightly negative NAT values for P1 in all the EA countries  
238 compared to positive trends during P2. Consequently, SATs in EA remained relatively stable during P1  
239 ( $-0.003\text{ }^{\circ}\text{C/decade}$ ) in P1 and P2 ( $0.019\text{ }^{\circ}\text{C/decade}$ ) in response to NAT forcing. The increasing trends during P2 can  
240 be attributed to the third industrial revolution. The third industrial revolution (1969–2000) was most prominent in the  
241 region of China, Japan, and Korea, where significant development took place (for example, new industries and  
242 technologies were established) (Janicke and Jacob 2013; Lixing 2013; Wen 2016). Thus, the surface temperature  
243 increased significantly over EA and the global climate was also affected (figure not shown). Tett et al. (2002) also  
244 found that temperatures increased by 0.1 K from 1900–1960 and then subsequently (1960–1997) increased by 0.5 K,  
245 owing to anthropogenic effects over the global scale. GHG forcing produced the strongest warmest trend among all  
246 the forcings (Figure 2d) corresponding to  $0.082\text{ }^{\circ}\text{C/decade}$  across all of EA during P1 and  $0.268\text{ }^{\circ}\text{C/decade}$  during P2.  
247 Mongolia, China, Korea, and Japan showed higher warming rates as a result of GHG forcing during P2 than during  
248 P1 (Table 2). A significant increase in GHG forcing effects can be seen for P2, again indicating the impact of  
249 industrialization during this period. The SOL forcing effects (Figure 2e) show mostly stable trends during P1 and P2,  
250 with values of  $0.005$  and  $0.008\text{ }^{\circ}\text{C/decade}$  for the entire EA region, respectively. The average temperature trends in  
251 response to LU forcing are shown in Table 2 for each EA region, which associated with warming trends. Across all  
252 of EA, LU increased SATs by  $0.084$  and  $0.239\text{ }^{\circ}\text{C/decade}$  during P1 and P2, respectively. Over EA, LU changes  
253 caused significant temperature increases owing to a reduction of plant transpiration after deforestation and  
254 desertification; i.e., changes from forest to shrubland or cropland lead to increases in sensible heat flux and drying of  
255 the soil (Gao et al. 2003). LU changes can also reduce precipitation (Dale 1997). These trends further indicate an  
256 enhanced warming rate after industrialization (P2).

257 The MME mean responses of ALL, GHG, LU, AER, NAT, and SOL of each forcing was averaged for each  
258 EA country as well as for the whole of EA. The annual temperature anomalies for each forcing were calculated relative  
259 to the 1850–2019 period; anomalies were also estimated for 1850–2014, which was the period for which ALL forcing  
260 simulations were available. Figure 3 shows the temperature anomalies of ALL forcings as well as ground observations,

261 CRU (1901–2018), and HadCRUT4 (1850–2019) for all of EA and each country. Based on these results, the SAT  
262 trends associated with ALL forcings were consistent with the observed trends. The SATs in the HadCRUT4 and ALL  
263 datasets were mostly stable between 1850 and 1900, after which SAT dropped. This may have been caused by the  
264 cooling effect of AER. From 1901 to 1970, the observations (CRU and HadCRUT4) and the ALL data anomalies  
265 show slow increasing SAT trends. However, from 1970 to 2014/2019, SAT increased rapidly owing to the third  
266 industrial revolution. Across all of EA, SAT had increased by 1.5 °C by 2019, with trends in each country being  
267 broadly similar. Specifically, under the ALL forcings, all the East Asian countries experienced smaller increments of  
268 change between 1900 and 1969 compared to a higher rate of increase between 1970 and 2014. By 2019, the SATs in  
269 China and Japan had increased by  $\geq 1$  °C, while in Korea and Mongolia, the increase had reached  $\geq 1.5$  °C. The SAT  
270 anomaly response to GHG forcing is shown in Figure 4 for the period 1850–2019, with observational and simulated  
271 SAT datasets showing a similar increasing trend. A slow increase in GHG forcing is observed until 1969, after which  
272 SATs begin to increase very rapidly. Indeed, GHG forcing has been the dominant contributor to the observed SAT  
273 warming in each country as well as across the whole of EA. For example, GHG forcing increased SATs by  
274 approximately 1.9 °C throughout EA and China by 2019, with even higher degrees of warming ( $\geq 2$  °C) in Mongolia  
275 and Korea. In Japan the equivalent temperature increase was  $\leq 2$  °C. In response to LU forcing, SAT warming rates  
276 closely match the CRU/HadCRUT4 observations (Figure S1 in Supplementary material). The temperature trend  
277 response to AER forcing was negative throughout EA and in each country (Figure 5), indicating that the cooling effect  
278 of AER forcing partially counteracts the warming caused by other forcings. The SAT changes in response to the NAT  
279 and SOL forcings are shown in Figures 6 and S2 (Supplementary material), respectively, which remained broadly  
280 stable in all the EA regions indicating minimal forcing effects.

281 Table 3 shows the correlations between the SAT trends of the observed data (CRU) and the response to  
282 different forcings based on the CMIP6 historical models. The SAT response to LU is strongly correlated with the CRU  
283 SAT data, and ALL and GHG also show positive correlations. In contrast, AER is negatively correlated with the CRU  
284 data, and NAT and SOL show very weak/no correlation. These correlations clearly demonstrate the direction (i.e.,  
285 warming or cooling) and relative strength of the contributions of the different forcing factors to SAT changes over the  
286 entire study period. Specifically, ALL, GHG, and LU forcings are associated with SAT increases; AER forcing  
287 produced a cooling effect; and NAT and SOL forcings had very weak or no impact on the warming rate.

## 288 3.2 Detection and attribution analysis

289 We conducted detection and attribution analysis based on the ROF method for the annual mean temperature  
290 in EA over the last 110 years (1905–2014). The scaling factors, with 90% confidence intervals, of the one-, two-, and  
291 three-signal analyses are presented in Figure 7. One-signal analyses were performed on the individual forcings of ALL  
292 (best estimate 1.16 with 90% confidence interval of 0.85 to 1.47) and ANT (best estimate 1.21 with 90% confidence  
293 interval of 0.9 to 1.56), as shown in Figure 7a. The 90% confidence intervals of ALL, and ANT are above zero,  
294 indicating that these forcings are robustly detected in EA. The best estimate of ALL is greater than unity indicates the  
295 observed changes were underestimated by MME mean in response to ALL. Furthermore, the best estimates of ALL ,  
296 and ANT are close to unity, indicating detection results pass the residual consistency test, which representing the good  
297 agreement between model simulations and observed changes. The two-signal analyses were performed on the ANT  
298 (best estimate 1.24 with 90% confidence interval of 0.91 to 1.57) and NAT (best estimate 0.16 with 90% confidence  
299 interval of -1.32 to 1.66) forcings, the scaling factors of which are shown in Figure 7b with 90% confidence intervals.  
300 The best estimates of ANT (1.24) and NAT (0.16) suggests that the effect of ANT can be separated from NAT. Further,  
301 ANT is robustly detected in EA, with a 90% confidence interval above zero; the best estimate is close to unity and is  
302 also comparable with ANT in the one-signal analysis, implying the robustness of anthropogenic influence on the  
303 observed temperature changes. In comparison, the lower bound of the NAT forcing is below zero, indicating that this  
304 forcing is undetected in EA. Therefore, only anthropogenic forcing can explain the observed annual mean temperature  
305 changes in EA from 1905 to 2014.

306 We conducted the three-signal analyses using GHG (best estimate 0.89 with 90% confidence interval of 0.48  
307 to 1.29), ANTnoGHG (best estimate 0.77 with 90% confidence interval of -0.54 to 2.1), and NAT (best estimate 0.68  
308 with 90% confidence interval of -0.82 to 2.21) to determine the major contributors among the anthropogenic forcings  
309 or other factors causing changes in the observations. This analysis also explored the influence of GHG forcing on SAT  
310 variations. Figure 7c shows the scaling factors for GHG, ANTnoGHG, and NAT. GHG is robustly detected in EA,  
311 with a 90% confidence interval above zero and a best estimate close to unity, which implies good agreement with the  
312 observations. In contrast, the lower bounds of the ANTnoGHG and NAT forcing include zero indicate that these are  
313 not detected in EA. Therefore, GHG forcing can be separated from ANTnoGHG and NAT forcing, and is considered  
314 the dominant anthropogenic factor forcing for the observed temperature changes in the study region.

### 315 3.3 Observation-constrained future projections

316 The one-signal analysis shown in Figure 7a demonstrates that the best estimate of ALL forcings is 1.16  
317 (above 1), indicating an underestimation of the CMIP6 historical simulations. This historical underestimation could  
318 continue in future projections, requiring appropriate adjustment/correction to ensure the accurate estimation of future  
319 scenarios. Therefore, the MME mean future projections under the low SSP1–2.6 and SSP2–4.5, and high SSP5–8.5,  
320 scenarios were multiplied by the best estimate of the ALL forcing scaling factor obtained in the one-signal analysis.  
321 Figure 8a shows the resulting historic (1850–2014) and future scenarios (2015–2100) for EA. These observation-  
322 constrained future projections show higher warming rates than the raw simulations. The adjusted/best estimate of the  
323 future projections of SSP1–2.6, SSP2–4.5, and SSP5–8.5 show temperature increases of 2.32 °C (90% confidence  
324 interval: 1.80–3.15 °C), 2.46 °C (90% confidence interval: 1.78–3.16 °C), and 3.12 °C (90% confidence interval:  
325 2.55–3.90 °C), respectively by 2050 compared to 1.92 °C, 2.12 °C, and 2.68 °C based on the unadjusted simulations,  
326 respectively; by 2070, the best estimate temperature increases under SSP1–2.6, SSP2–4.5, and SSP5–8.5 are 2.64 °C  
327 (90% confidence interval: 1.97–3.29 °C), 3.10 °C (90% confidence interval: 2.34–3.89 °C), and 4.61 °C (90%  
328 confidence interval: 4.17–5.28 °C), respectively, compared to 2.28 °C, 2.64 °C, and 3.95 °C based on the original  
329 simulations; and by 2100, the best estimates under the same three scenarios are 2.49 °C (90% confidence interval:  
330 1.84–3.12 °C), 3.66 °C (90% confidence interval: 3.07–4.27 °C), and 7.22 °C (90% confidence interval: 6.79–8.15 °C)  
331 compared to 2.17 °C, 3.15 °C, and 6.19 °C based on the original simulations, respectively. We also estimated the best  
332 values for the ALL forcing scaling factors for each EA country and generated projections for each EA country. The  
333 best estimates for the ALL forcing scaling factors, with 90% confidence intervals, for each EA country are shown in  
334 Table 4. The country-scale future projections under each of the scenarios were adjusted based on their respective ALL  
335 forcing best estimates, as shown in Figures 8b–e. The best estimates of the future projections of SSP1–2.6, SSP2–4.5,  
336 and SSP5–8.5, with 90% confidence intervals, for each EA country in 2050, 2070, and 2100 are shown in Table 5.  
337 The resulting observation-constrained future projections in all the EA countries show higher warming rates relative  
338 to the raw simulation data, and warming is projected to increase over time.

### 339 4. Summary and conclusions

340 This study describes long-term SAT changes in EA using the new state-of-the-art CMIP6 multi-model  
341 simulations. These model simulations were validated in comparison with CRU/HadCRUT4 observational

342 measurements. The SAT variation responses to various external and natural forcings (ALL, AER, NAT, GHG, SOL,  
343 and LU) were examined between 1850 and 2014/2019. Throughout EA, southeast China has experienced the highest  
344 mean temperatures (approximately 25 °C) compared to the lowest on the Tibetan Plateau (approximately -12 °C).  
345 SATs during the study period were increased due to GHG and LU forcings and decreased due to the AER forcing. In  
346 contrast, NAT and SOL had little impact on SAT changes. GHG forcing was the dominant factor in the observed  
347 temperature increase. Overall, the SAT in EA increased by 0.082 °C/decade in response to the GHG forcing, compared  
348 to 0.031 °C/decade under ALL forcings from 1850–2014. After the third industrial revolution, SATs increased very  
349 rapidly, by 0.268 and 0.255 °C/decade in response to the GHG and ALL forcings, respectively, between 1970 and  
350 2014 (Tett et al. 2002). By 2019, the GHG forcing had increased the SAT across the EA by approximately 1.9 °C, and  
351 all countries in EA had also experienced increasing SAT trends as a result of anthropogenic forcings (GHG, and LU).

352 Overall, Mongolia experienced faster rates of temperature rise than other EA countries; however, throughout  
353 EA, the highest and lowest amounts of warming occurred in Tibet and southeast China, respectively. The strongest  
354 cooling response to AER forcing occurred in southeast China, while across EA, the overall cooling rate associated  
355 with AER forcing was approximately -0.076 °C/decade between 1850 and 2014. Interestingly, in Mongolia, AER  
356 showed a warming rather than cooling influence during the 1971–2014 period, which might partially explain the high  
357 degree of warming in this region. Across EA, LU increased the temperature by 0.084 °C, between 1850 and 2014,  
358 while NAT and SOL forcings had a minimal effect overall. The changes in LU increased the temperature owing to  
359 reduced vegetation cover and desertification. Based on these observations, anthropogenic forcing has significantly  
360 influenced the climate of EA, associated with distinct warming trends. Furthermore, we present future SAT projections  
361 up to 2100 based on the low SSP1–2.5 and SSP2–4.5, and high SSP5–8.5, scenarios.

362 We applied the ROF detection and attribution technique to CMIP6 simulations to describe climate change in  
363 EA resulting from anthropogenic influences. The ALL and ANT forcings were robustly detected from the one-signal  
364 analyses for the period 1905–2014; in the two-signal analysis, ANT and NAT influences could be separated, and the  
365 ANT forcing was clearly detected as a factor including the increase in SATs; and in the three-signal analysis, GHG  
366 forcing was separated from ANTnoGHG and NAT forcings and was strongly detected, indicating that GHG forcing  
367 was the dominant factor driving climate change in EA. Finally, we generated adjusted/corrected future warming trends  
368 by multiplying the raw simulation data with the ALL forcing best estimates, which produced higher projected

369 temperature values under the SSP1–2.5, SSP2–4.5, and SSP5–8.5 scenarios. Overall, we conclude that the climate  
370 (SAT) changes observed in EA are the result of anthropogenic forcings, primarily GHG and LU. This implies that  
371 efforts to mitigate future climate change in this region should focus on these anthropogenic forcing factors.

### 372 **Funding**

373 This work was supported by the Korea Institute of Civil Engineering and Building Technology Strategic Research  
374 Project (Establishment of 3D Fine Dust Information Based on AI Image Analysis).

### 375 **Conflicts of interest**

376 The authors declare no conflict of interest.

### 377 **Availability of data and material**

378 The datasets were used in the present study are HadCRUT4 available at <https://crudata.uea.ac.uk/cru/data/temperature/>;  
379 CRU available at <https://crudata.uea.ac.uk/cru/data/hrg/>; and CMIP6 available at [https://esgf-](https://esgf-node.llnl.gov/projects/cmip6/)  
380 [node.llnl.gov/projects/cmip6/](https://esgf-node.llnl.gov/projects/cmip6/).

### 381 **Code availability**

382 The code for regularized optimal fingerprinting method used for detection and attribution analysis is available at  
383 <http://www.umr-cnrm.fr/spip.php?article23&lang=en>.

### 384 **Authors' contributions**

385 Shaik Allabakash performed data analyses and conceptualization and wrote the first manuscript draft. Sanghun Lim  
386 provided helpful discussions on the analyses of data, conceptualization, methodology, and review and edited the  
387 manuscript.

### 388 **Acknowledgments**

389 This work was supported by the Korea Institute of Civil Engineering and Building Technology Strategic Research  
390 Project (Establishment of 3D Fine Dust Information Based on AI Image Analysis). We acknowledge the World  
391 Climate Research Program for making the CMIP6 dataset available for global- and regional-scale climate research.  
392 The authors would like to thank the National Climate Center, Research, for providing the CRU dataset.

393

394 **References**

- 395 Allen MR, Stott PA (2003) Estimating signal amplitudes in optimal fingerprinting, Part I: Theory. *Clim*  
396 *Dynam* 21:477-491.
- 397 Allen MR, Tett SF (1999) Checking for model consistency in optimal fingerprinting. *Clim Dynam* 15:419-434.
- 398 Almazroui M, Islam MN, Saeed F., Saeed S, Ismail M, Ehsan MA, Diallo I, O'Brien E, Ashfaq M, Martínez-Castro  
399 D, Cavazos T (2021) Projected changes in temperature and precipitation over the United States, Central America, and  
400 the Caribbean in CMIP6 GCMs. *Earth Syst Environ* 5:1-24.
- 401 Almazroui M, Saeed S, Saeed F, Islam MN, Ismail M (2020) Projections of precipitation and temperature over the  
402 South Asian countries in CMIP6. *Earth Syst Environ* 4:297-320.
- 403 Bindoff NL, Stott PA, AchutaRao KM, Allen MR, Gillett N, Gutzler D, Hansingo K, Hegerl G, Hu Y, Jain S, Mokhov  
404 II (2013) Detection and attribution of climate change: from global to regional. The Intergovernmental Panel on Climate  
405 Change (IPCC).
- 406 Burke C, Stott P, Sun Y, Ciavarella A (2016) Attribution of extreme rainfall in Southeast China during May 2015. In:  
407 Explaining Extreme Events of 2015 from a Climate Perspective. *Bull Am Meteorol Soc* 97:S92-S96.
- 408 Chen L, Chen X, Cheng L, Zhou P, Liu Z (2019) Compound hot droughts over China: identification, risk patterns and  
409 variations. *Atmos Res* 227:210-219.
- 410 Chung YS, Yoon MB (2000) Interpretation of recent temperature and precipitation trends observed in Korea. *Theor*  
411 *Appl Climatol* 67:171-180.
- 412 Dale VH (1997) The relationship between land-use change and climate change. *Ecol Appl* 7:753-769.
- 413 Drumond A, Stojanovic M, Nieto R, Gimeno L, Liberato ML, Pauliquevis T, Oliveira M, Ambrizzi T (2021) Dry and  
414 wet climate periods over eastern South America: identification and characterization through the SPEI  
415 index. *Atmosphere*, 12:155.
- 416 Egorova T, Rozanov E, Arsenovic P, Peter T, Schmutz W (2018) Contributions of natural and anthropogenic forcing  
417 agents to the early 20th century warming. *Front Earth Sci* 6:206.

418 Eyring V, Bony S, Meehl GA, Senior CA, Stevens B, Stouffer RJ, Taylor KE (2016) Overview of the Coupled Model  
419 Intercomparison Project Phase 6 (CMIP6) experimental design and organization. *Geosci Model Dev* 9:1937-1958.

420 Fujibe F (2009) Detection of urban warming in recent temperature trends in Japan. *Int J Climatol* 29:1811-1822.

421 Gao XJ, Luo Y, Lin WT, Zhao ZC, Giorgi F (2003) Simulation of effects of land use change on climate in China by  
422 a regional climate model. *Adv Atmos Sci* 20:583-592.

425 Harris I, Osborn TJ, Jones P, Lister D (2020) Version 4 of the CRU TS monthly high-resolution gridded multivariate  
426 climate dataset. *Sci Data* 7:1-18.

427 Janicke M, Jacob K (2013) A third industrial revolution. In: Siebenhüner B, Arnold M, Eisenack K, Jacob KH (eds)  
428 Long-term governance for social-ecological change. Routledge, New York, pp 47-71.

429 Jones GS, Stott PA, Christidis N (2013) Attribution of observed historical near-surface temperature variations to  
430 anthropogenic and natural causes using CMIP5 simulations. *J Geophys Res: Atmos* 118:4001-4024.

431 Jung HS, Choi Y, Oh JH, Lim GH (2002) Recent trends in temperature and precipitation over South Korea. *Int J*  
432 *Climatol* 22:1327-1337.

433 Li H, Chen H, Wang H (2017) Effects of anthropogenic activity emerging as intensified extreme precipitation over  
434 China. *J Geophys Res: Atmos* 122:6899-6914.

435 Li K, Liao H, Cai W, Yang Y (2018a) Attribution of anthropogenic influence on atmospheric patterns conducive to  
436 recent most severe haze over eastern China. *Geophysical Research Letters*, 45:2072-2081.

437 Li D, Zhou T, Zou L, Zhang W, Zhang L (2018b) Extreme high-temperature events over East Asia in 1.5 °C and 2 °C  
438 warmer futures: analysis of NCAR CESM low-warming experiments. *Geophys Res Lett* 45:1541-1550.

439 Lixing Z (2013) The third industrial revolution and development strategies of China. In: International affairs forum,  
440 Vol 4. Routledge, New York, pp. 79-82.

441 Lu C, Sun Y, Wan H, Zhang X, Yin H (2016) Anthropogenic influence on the frequency of extreme temperatures in  
442 China. *Geophys Res Lett* 43:6511-6518.

443 Ma S, Zhou T, Stone DA, Polson D, Dai A, Stott PA, von Storch H, Qian Y, Burke C, Wu P, Zou L (2017) Detectable  
444 anthropogenic shift toward heavy precipitation over eastern China. *J Clim* 30:1381-1396.

445 Meehl GA, Washington WM, Ammann CM, Arblaster JM, Wigley TML, Tebaldi C (2004) Combinations of natural  
446 and anthropogenic forcings in twentieth-century climate. *J Clim* 17:3721-3727.

448 Om KC, Ren G, Jong SI, Li S, Kang-Chol O, Ryang CH, Zhang P (2019) Long-term change in surface air temperature  
449 over DPR Korea, 1918–2015. *Theor Appl Climatol* 138: 363-372.

450 Paik S, Min SK (2020) Quantifying the anthropogenic greenhouse gas contribution to the observed spring snow-cover  
451 decline using the CMIP6 multimodel ensemble. *J Clim* 33:9261-9269.

452 Paik S, Min SK, Zhang X, Donat MG, King AD, Sun Q (2020) Determining the anthropogenic greenhouse gas  
453 contribution to the observed intensification of extreme precipitation. *Geophys Res Lett* 47:e2019GL086875.

454 Peng S, Gang C, Cao Y, Chen Y (2018) Assessment of climate change trends over the Loess Plateau in China from  
455 1901 to 2100. *Int J Climatol* 38:2250-2264.

456 Qian W, Qin A (2006) Spatial-temporal characteristics of temperature variation in China. *Meteorol Atmos Phys* 93:1-  
457 16.

458 Qian C, Wang J, Dong SY, Yin H, Burke C, Ciavarella A, Dong B, Freychet N, Lott FC, Tett SF (2018) Human  
459 influence on the record-breaking cold event in January of 2016 in eastern China. In: Herring SC, Christidis N, Hoell  
460 A, Kossin JP, Schreck CJ III, and Stott PA (eds) *Explaining extreme events of 2016 from a climate perspective*. *Bull*  
461 *Am Meteorol Soc* 99:S118-S122.

462 Ribes A, Planton S, Terray L (2013) Application of regularised optimal fingerprinting to attribution. Part I: method,  
463 properties and idealised analysis. *Clim Dynam* 41:2817-2836.

464 Ribes A, Terray L (2013) Application of regularised optimal fingerprinting to attribution. Part II: application to global  
465 near-surface temperature. *Clim Dynam* 41:2837-2853.

466 Santer BD, Taylor KE, Gleckler PJ, Bonfils C, Barnett TP, Pierce DW, Wigley TML, Mears C, Wentz FJ, Brüggemann  
467 W, Gillett NP (2009) Incorporating model quality information in climate change detection and attribution studies. *Proc*  
468 *Natl Acad Sci* 106:14778-14783.

469 Song L, Sun Y, Dong S, Zhou B, Stott P, Ren G (2015) Role of anthropogenic forcing in 2014 hot spring in northern  
470 China. *Bull Am Meteorol Soc* 96:S111- S114.

471 Stocker TF, Qin D, Plattner GK, Tignor MM, Allen SK, Boschung J, Nauels A, Xia Y, Bex V, Midgley PM (2014)  
472 *Climate Change 2013: the physical science basis. Contribution of working group I to the fifth assessment report of the*  
473 *IPCC, the intergovernmental panel on climate change. Cambridge University Press, Cambridge and New York.*

474 Stott PA, Gillett NP, Hegerl GC, Karoly DJ, Stone DA, Zhang X, Zwiers F (2010) Detection and attribution of climate  
475 change: a regional perspective. *WIREs: Clim Change* 1:192-211.

476 Street JO, Carroll RJ, Ruppert D (1988) A note on computing robust regression estimates via iteratively reweighted  
477 least squares. *Am Stat* 42:152-154.

478 Sun Y, Song L, Yin H, Zhang X, Stott P, Zhou B, Hu T (2016) Human influence on the 2015 extreme high temperature  
479 events in Western China. *Bull Am Meteorol Soc* 97:S102-S106.

480 Tang G, Ding Y, Wang S, Ren G, Liu H, Zhang L (2010) Comparative analysis of China surface air temperature series  
481 for the past 100 years. *Adv Clim Change Res* 1:11-19.

482 Tett SF, Jones GS, Stott PA, Hill DC, Mitchell JF, Allen MR, Ingram WJ, Johns TC, Johnson CE, Jones A, Roberts  
483 DL (2002) Estimation of natural and anthropogenic contributions to twentieth century temperature change. *J Geophys*  
484 *Res: Atmos* 107:ACL-10.

485 Tokarska KB, Hegerl GC, Schurer AP, Ribes A, Fasullo JT (2019) Quantifying human contributions to past and future  
486 ocean warming and thermosteric sea level rise. *Environ Res Lett* 14:074020.

487 Wang L, Wu Z, Wang F, Du H, Zong S (2016) Comparative analysis of the extreme temperature event change over  
488 Northeast China and Hokkaido, Japan from 1951 to 2011. *Theor Appl Climatol* 124:375-384.

489 Wang Y, Sun Y, Hu T, Qin D, Song L (2018) Attribution of temperature changes in Western China. *Int J*  
490 *Climatol* 38:742-750.

491 Weller E, Min SK, Palmer MD, Lee D, Yim BY, Yeh SW (2016) Multi-model attribution of upper-ocean temperature  
492 changes using an isothermal approach. *Sci Rep* 6:1-10.

493 Wen Y (2016) China's rapid rise. Federal Reserve Bank of St. Louis. Reg Econ 24:8-14.

494 Xu Y, Gao X, Shi Y, Botao Z (2015) Detection and attribution analysis of annual mean temperature changes in  
495 China. Clim Res 63:61-71.

496 Xuejie G, Zongci Z, Giorgi F (2002) Changes of extreme events in regional climate simulations over East Asia. Adv  
497 Atmos Sci 19:927-942.

498 Yin H, Sun Y, Wan H, Zhang X, Lu C (2017) Detection of anthropogenic influence on the intensity of extreme  
499 temperatures in China. Int J Climatol 37:1229-1237.

500 Yoon D, Cha DH, Lee G, Park C, Lee MI, Min KH (2018) Impacts of synoptic and local factors on heat wave events  
501 over southeastern region of Korea in 2015. J Geophys Res: Atmos 123:12-081.

502 Yoon D, Cha DH, Lee MI, Min KH, Kim J, Jun SY, Choi Y (2020) Recent changes in heatwave characteristics over  
503 Korea. Climate Dynamics 55:1685-1696.

504 Zeng Y, Zhou Z, Yan Z, Teng M, Huang C (2019) Climate change and its attribution in three gorges reservoir area,  
505 China. Sustainability 11:7206.

506 Zhang J, Zhao T, Dai A, Zhang W (2019) Detection and attribution of atmospheric precipitable water changes since  
507 the 1970s over China. Sci Rep 9:1-10.

508 Zhou L, Dickinson RE, Tian Y, Fang J, Li Q, Kaufmann RK (2004) Evidence for a significant urbanization effect on  
509 climate in China. Proc Natl Acad Sci 101:9540-9544.

510

511

512

513

514

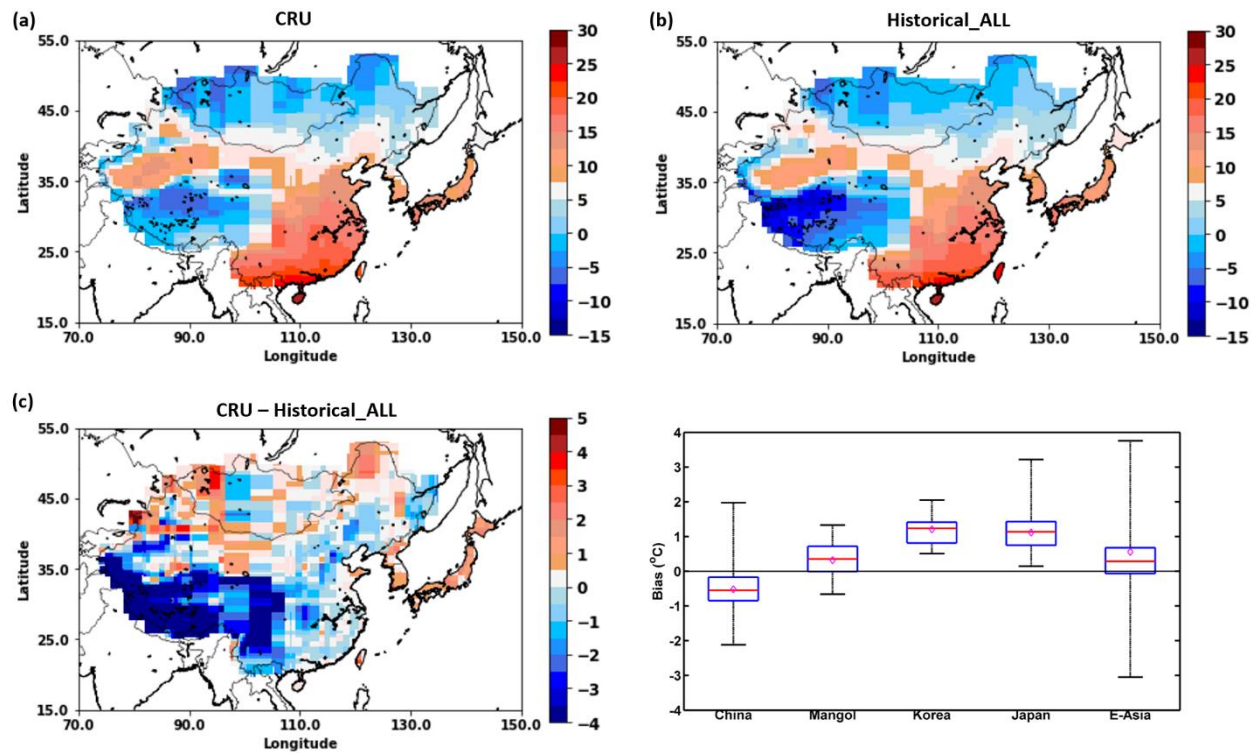
515

516

517

518

519



520

521 **Fig. 1** Annual mean temperatures from 1901 to 2014. (a) CRU, (b) Multi-model ensemble mean of surface air  
 522 temperature responses to ALL (anthropogenic and natural) forcing obtained from CMIP6. (c) Bias between CRU and  
 523 CMIP6 (CMIP6 – CRU) across EA. (d) Bias (CMIP6 – CRU) boxplots showing 5%, 25%, mean (diamond), 75%,  
 524 and 95% values

525

526

527

528

529

530

531

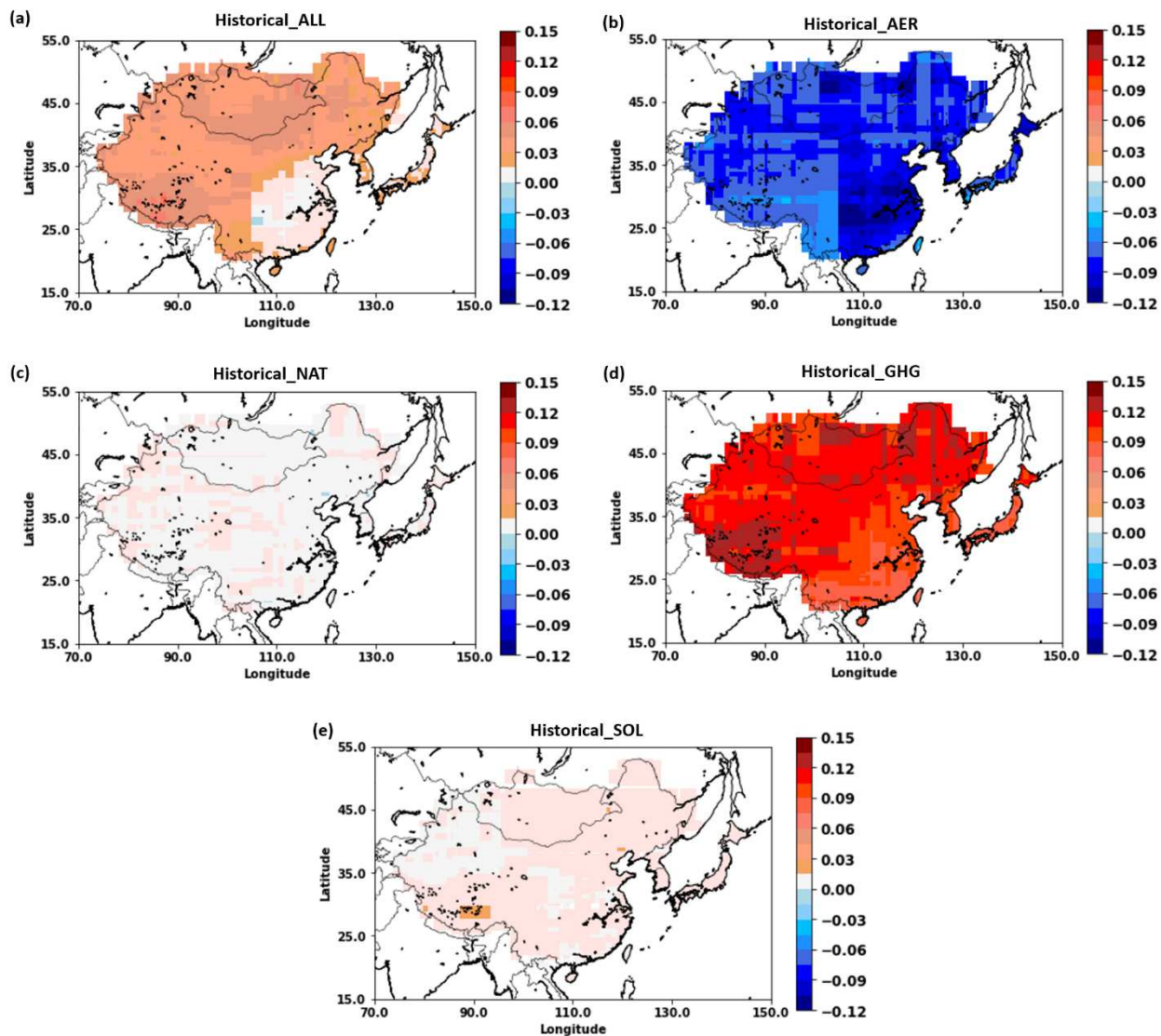
532

533

534

535

536



537

538 **Fig. 2** Spatial distribution of trends in annual mean surface air temperature responses to different forcings (°C/decade)  
539 for the historical period 1850–2014. (a) all (ALL), (b) anthropogenic aerosol (AER), (c) natural (NAT), (d) greenhouse  
540 gas (GHG), and (e) solar irradiance (SOL) forcings. The trends are estimated based on robust regression analysis

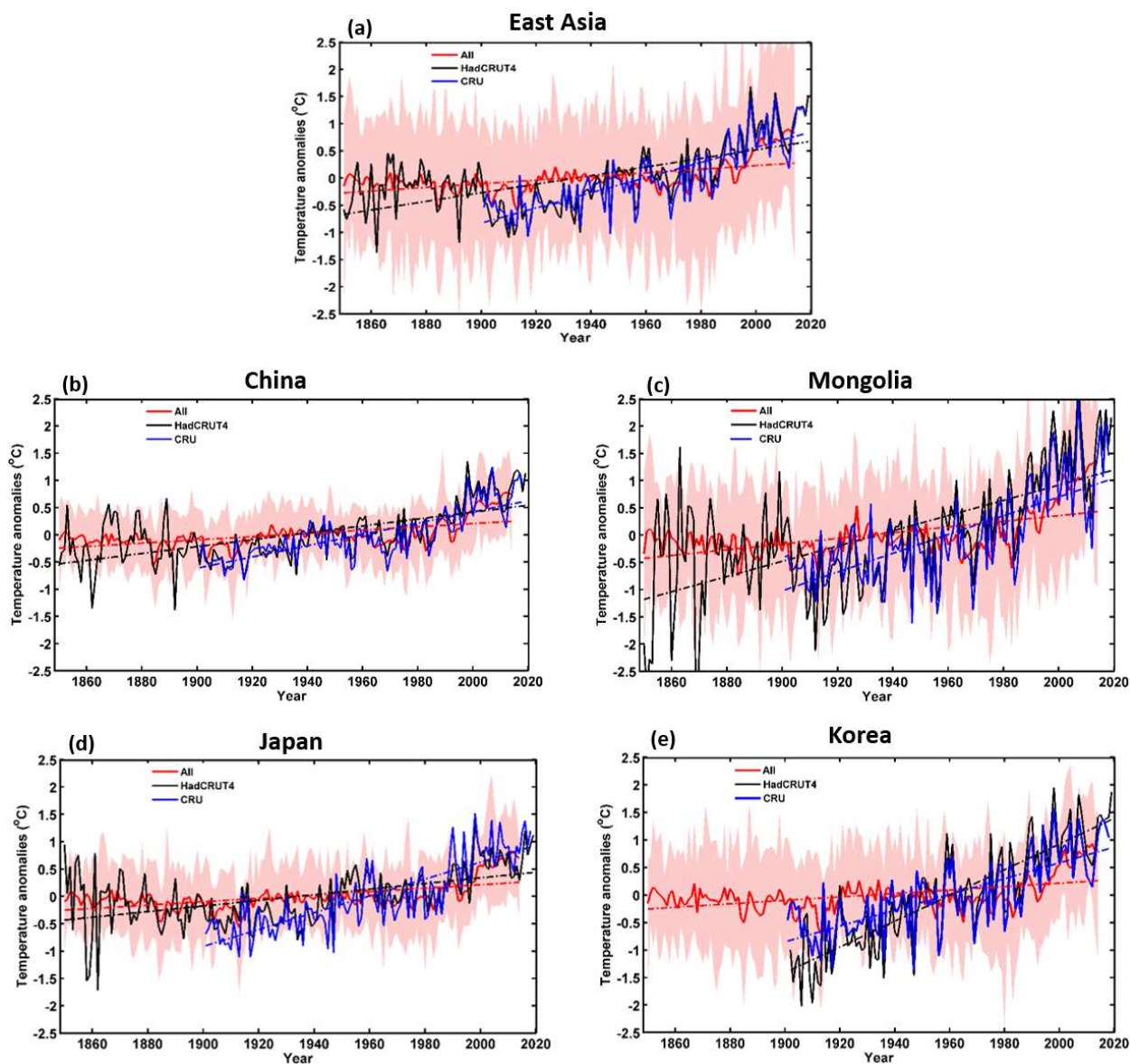
541

542

543

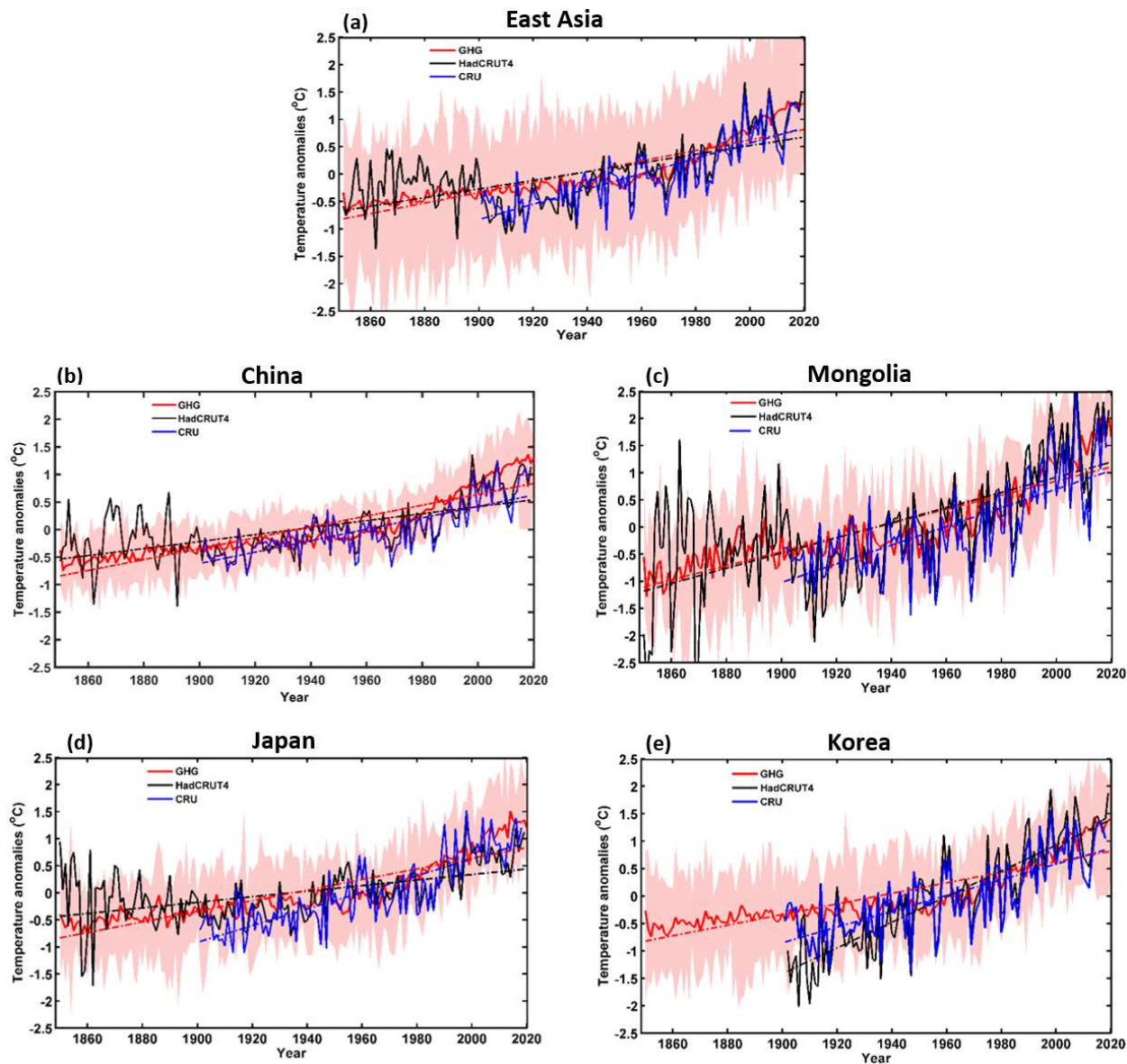
544

545



547

548 **Fig. 3** Temporal variation of annual mean temperature anomaly responses to ALL (all forcings) averaged across East  
 549 Asia and individual countries from observations (CRU and HadCRUT4) and multi-model mean simulations (CMIP6)  
 550 for the period 1850–2014 (CRU: 1901–2018, HadCRUT4: 1850–2019). Shaded bands are multi-model ranges



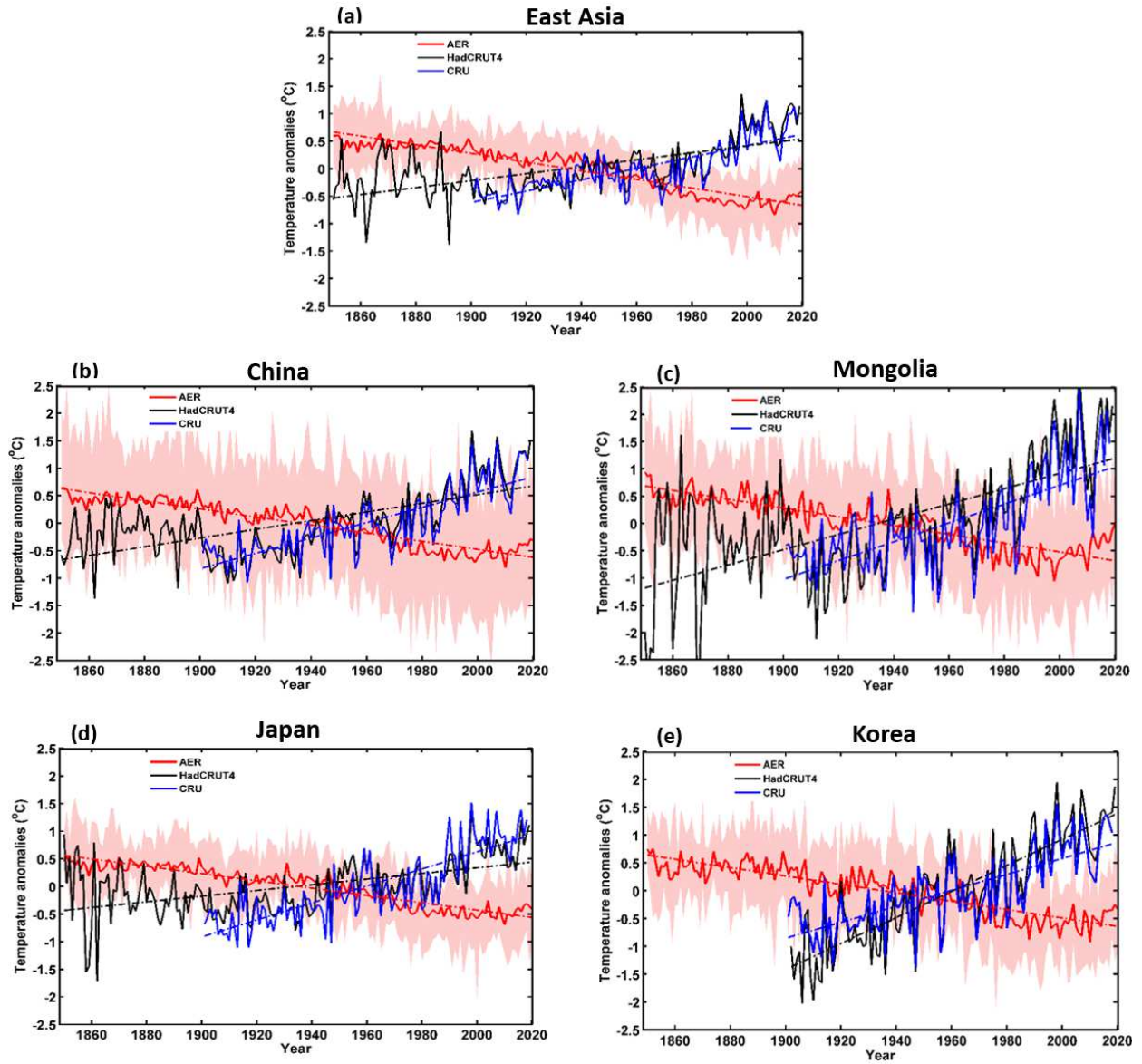
552

553 **Fig. 4** As for Figure 3 but showing temperature anomaly responses to GHG forcing

554

555

556

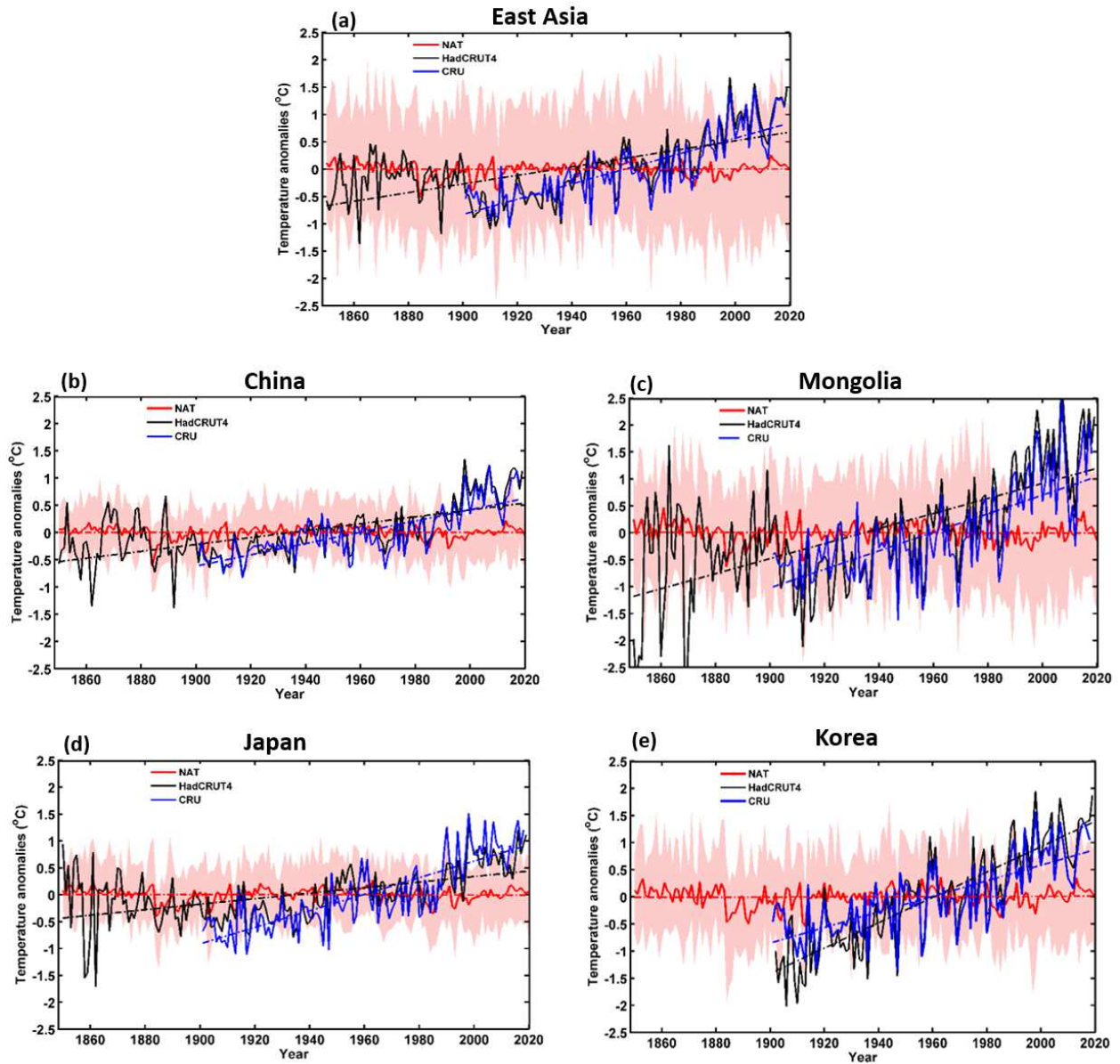


557

558

559

**Fig. 5** As for Figure 3 but showing temperature anomaly responses to aerosol (AER) forcing

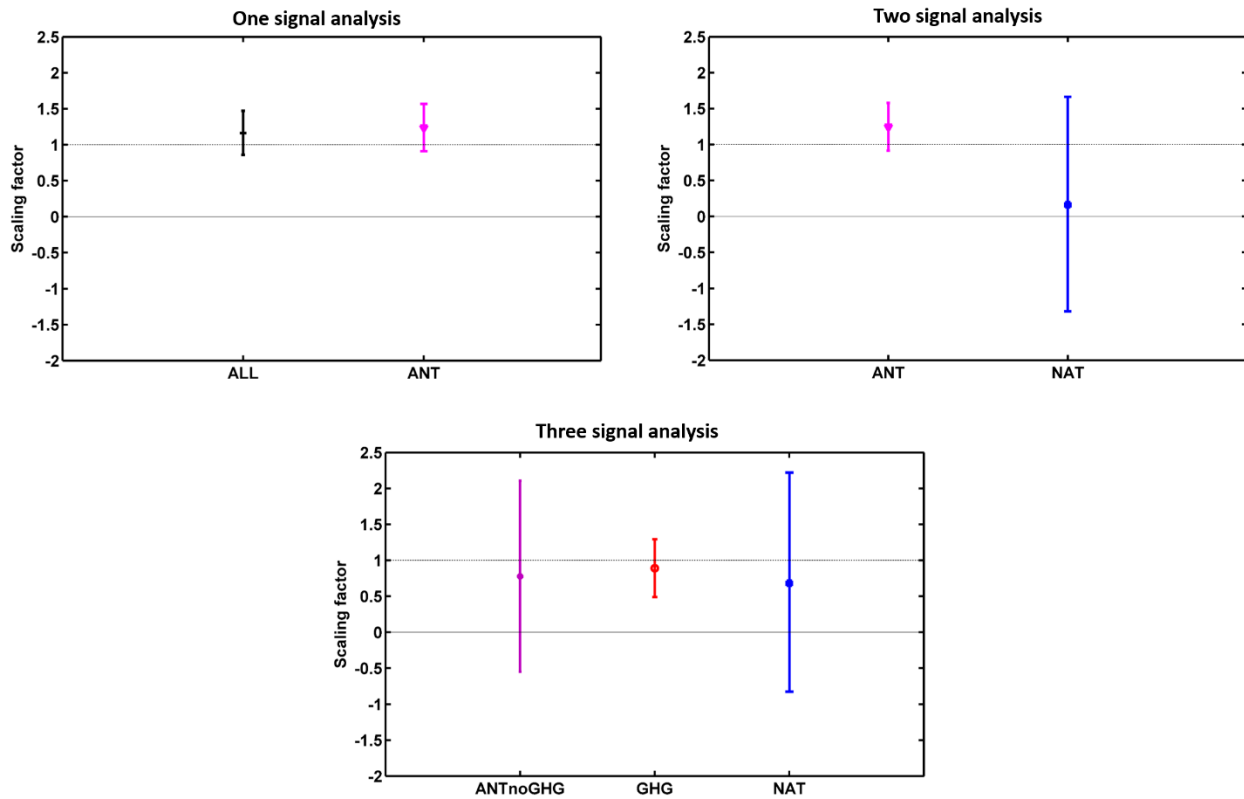


560

561 **Fig. 6** As for Figure 3 but showing temperature anomaly responses to natural (NAT) forcing

562

563



564

565 **Fig. 7** Best estimates of the scaling factors using the regularized optimal fingerprinting method with 90% confidence  
 566 intervals over EA for the period 1905–2014. (a) One-signal analysis of all (ALL) and anthropogenic aerosols (ANT)  
 567 forcings, (b) two-signal analysis of ANT and NAT forcings, (c) three-signal analysis of ANTnoGHG, GHG, and NAT

568

569

570

571

572

573

574

575

576

577

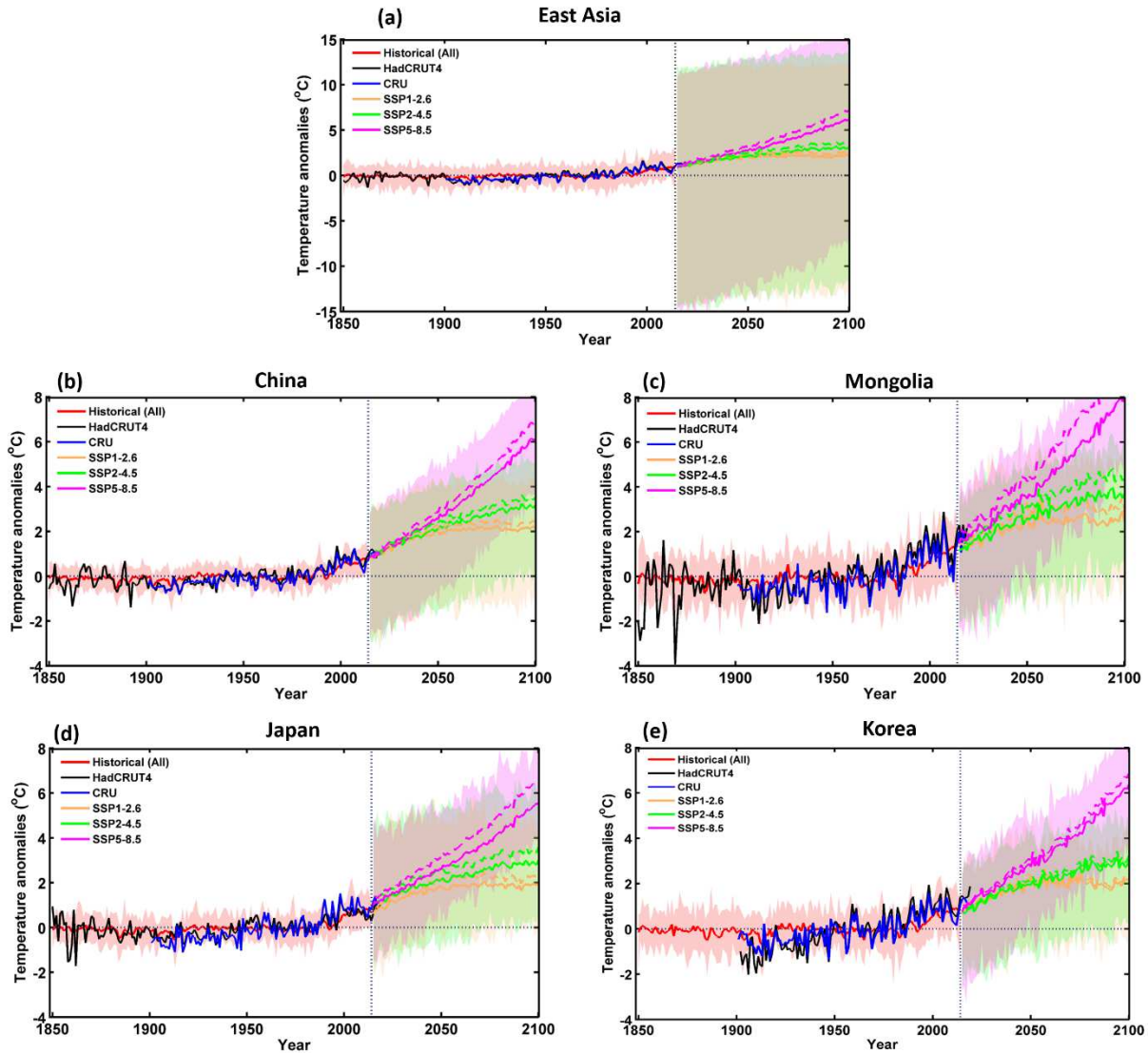
578

579

580

581

582



583

584 **Fig. 8** Temporal variations in annual SAT anomalies (relative to 1995–2014) during the period 1850–2100. Shaded  
 585 bands are the multi-model ranges. Future projections are based on the multi-model ensemble means under SSP1–2.6  
 586 (gold line), SSP2–4.5 (green line), and SSP5–8.5 (magenta line). The dashed lines indicate best-estimate observation-  
 587 constrained future temperature projections for (a) East Asia, (b) China, (c) Mongolia, (d) Japan, and (e) Korea  
 588

589

590

591

592

593

594

595

596

597

598

599

600 **Table 1** Models used in the study for historical and future projections (Y = ‘yes’ and ‘N’ = no). The numbers in  
601 parenthesis represent the ensemble sizes of the corresponding models

Model name	Historical forcing (1850–2014)						Future projection (2014–2100)			Control simulations
	ALL	AER	NAT	GHG	SOL	LU	SSP1-2.6	SSP2-4.5	SSP5-8.5	
CNRM-CM6-1-HR	Y (1)	N	N	N	N	N	Y (1)	Y (1)	Y (1)	N
CESM2-WACCM	Y (4)	N	N	Y (3)	N	Y (1)	Y (1)	Y (4)	Y (3)	Y (8)
E3SM-1-0	Y (5)	N	N	N	N	N	N	N	N	N
BCC-CSM2-MR	Y (3)	Y (3)	Y (3)	Y (3)	N	N	N	N	N	Y (15)
MRI-ESM2-0	Y (5)	Y (5)	Y (5)	Y (5)	Y (4)	N	Y (1)	Y (5)	Y (1)	Y (8)
CIESM	Y (3)	N	N	N	N	N	N	N	N	Y (20)
CAMS-CSM1-0	Y (3)	N	N	N	N	N	N	N	N	Y (16)
INM-CM4-8	Y (1)	N	N	N	N	N	Y (1)	Y (1)	Y (1)	Y (12)
FIO-ESM2-0	Y (3)	N	N	N	N	N	N	N	N	Y (15)
CMCC-CM2	Y (3)	N	N	N	N	N	N	N	N	Y (12)
HADGEM3-GC31-MM	Y (6)	N	N	N	N	N	Y (1)	N	Y (4)	Y (16)
MIROC6	Y (9)	Y (4)	Y (7)	Y (3)	Y (3)	Y (1)	Y (9)	N	Y (9)	N
GISS-E2-1-G	Y (8)	Y (6)	Y (5)	Y (5)	Y (6)	Y (5)	Y (5)	Y (6)	Y (2)	Y (12)
CNRM-CM6-1	Y (6)	N	Y (4)	Y (9)	N	Y (1)	Y (4)	Y (5)	Y (5)	Y (20)
IPSL-CM6A-LR	Y (4)	Y (9)	Y (9)	Y (4)	N	Y (1)	Y (3)	N	Y (6)	Y (6)
CNRM-ESM2-1	Y (3)	Y (2)	N	N	N	Y (1)	Y (4)	Y (5)	Y (4)	Y (16)
ACCESS-CM2	Y (3)	N	N	N	N	N	Y (3)	Y (3)	Y (3)	N
ACCESS-ESM1-5	Y (6)	Y (3)	Y (3)	Y (3)	N	N	Y (5)	Y (6)	Y (3)	N

HadGEM3- GC31-LL	Y (4)	Y (4)	Y (4)	Y (4)	N	N	Y (1)	Y (4)	Y (4)	Y (12)
UKESM1-0- LL	Y (6)	N	N	N	N	N	Y (4)	Y (6)	Y (3)	Y (10)
CanESM5	Y (5)	Y (9)	Y (5)	Y (6)	Y (9)	N	Y (3)	Y (5)	Y (4)	N
GFDL- ESM4	N	Y (1)	Y (3)	Y (1)	N	N	N	Y (3)	N	N
CMCC- ESM2	N	N	N	N	N	Y (1)	N	N	N	Y (16)
MPI-ESM1- 2-LR	N	N	N	N	N	Y (2)	Y (5)	Y (4)	Y (3)	Y (18)
CESM2	N	N	N	N	N	N	Y (3)	Y (3)	Y (3)	Y (20)
FGOALS- f3-L	N	N	N	N	N	N	N	Y (1)	N	Y (15)
NESM3	N	N	N	N	N	N	N	Y (2)	N	Y (8)
KACE-1-0- G	N	N	N	N	N	N	N	Y (3)	N	Y (8)
Total	21 (91)	10 (46)	10 (48)	11 (46)	4 (22)	8 (13)	17 (54)	18 (67)	17 (59)	21 (283)

602

603

604

605

606

607

608

609

610

611

612

613

614

615

616

617

618

619 **Table 2** Annual mean surface air temperature trend ( $^{\circ}\text{C}/\text{decade}$ ) responses to different forcings in each East Asian  
620 country and the entire EA region for the period 1850–2014 (P1) and 1971–2014 (P2, after third industrial revolution,  
621 shown in parenthesis). ALL = all, AER = anthropogenic aerosol, NAT = natural, GHG = greenhouse gas, SOL = solar  
622 irradiance, and LU = land use forcings

1850–2014 (1971–2014)	<b>East Asia</b>	<b>China</b>	<b>Mongolia</b>	<b>Japan</b>	<b>Korea</b>
<b>ALL</b>	0.031 (0.255)	0.027 (0.223)	0.049 (0.379)	0.026 (0.25)	0.029 (0.266)
<b>AER</b>	-0.076 (-0.035)	-0.081 (-0.058)	-0.086 (0.010)	-0.068 (-0.036)	-0.078 (-0.041)
<b>NAT</b>	-0.003 (0.019)	-0.0012 (0.013)	-0.002 (0.020)	-0.002 (0.015)	-0.002 (0.036)
<b>GHG</b>	0.082 (0.268)	0.090 (0.27)	0.1106 (0.328)	0.077 (0.240)	0.087 (0.278)
<b>SOL</b>	0.005 (0.008)	0.005 (-0.001)	0.006 (0.007)	0.005 (0.009)	0.005 (0.029)
<b>LU</b>	0.084 (0.239)	0.069 (0.235)	0.079 (0.327)	0.077 (0.200)	0.096 (0.218)

623  
624  
625  
626  
627  
628  
629  
630  
631  
632  
633  
634  
635  
636  
637  
638  
639  
640  
641  
642  
643  
644  
645  
646  
647  
648  
649  
650

651 **Table 3** Correlations between surface air temperature (SAT) in observed data (CRU) and SAT responses to different  
 652 forcings in CMIP historical models. ALL = all, AER = anthropogenic aerosol, NAT = natural, GHG = greenhouse  
 653 gas, SOL = solar irradiance, and LU = land use forcings  
 654

	<b>East Asia (CRU)</b>	<b>China (CRU)</b>	<b>Mongolia (CRU)</b>	<b>Japan (CRU)</b>	<b>Korea (CRU)</b>
<b>ALL</b>	0.69	0.76	0.62	0.70	0.53
<b>AER</b>	-0.68	-0.66	-0.55	-0.70	0.55
<b>NAT</b>	0.03	0.05	-0.03	0.01	0.06
<b>GHG</b>	0.77	0.77	0.70	0.75	0.65
<b>SOL</b>	0.08	0.10	0.006	0.09	0.04
<b>LU</b>	0.96	0.97	0.97	0.95	0.96

655  
 656  
 657  
 658  
 659  
 660  
 661  
 662  
 663  
 664  
 665  
 666  
 667  
 668  
 669  
 670  
 671

672 **Table 4** Best-estimate scaling factors and 90% confidence intervals (shown in parenthesis) of ALL (anthropogenic  
 673 and natural) forcing, estimated from one-signal analysis, in East Asian countries for the period 1905–2014

<b>1905– 2014</b>	<b>East Asia (90%)</b>	<b>China (90%)</b>	<b>Mongolia (90%)</b>	<b>Japan (90%)</b>	<b>Korea (90%)</b>
<b>ALL</b>	1.16 (0.85–1.47)	1.11 (0.85–1.38)	1.22 (1.01–1.44)	1.19 (0.86–1.51)	1.08 (0.71-1.45)

674  
 675  
 676  
 677  
 678  
 679  
 680  
 681  
 682  
 683  
 684  
 685  
 686  
 687  
 688  
 689  
 690  
 691  
 692  
 693  
 694  
 695  
 696  
 697  
 698  
 699

700 **Table 5** Best-estimates and 90% confidence intervals (shown in parenthesis) of future scenarios (SSP1-2.6, SSP2-4.5,  
701 and SSP5-8.5) in East Asian countries

<b>Future scenarios</b>	<b>Year</b>	<b>East Asia (90%)</b>	<b>China (90%)</b>	<b>Mongolia (90%)</b>	<b>Japan (90%)</b>	<b>Korea (90%)</b>
<b>SSP1-2.6</b>	2050	2.32 (1.80-3.15)	2.22 (1.57-2.87)	3.22 (2.38-4.07)	2.2 (1.63-2.76)	2.36 (1.71-3.01)
	2070	2.64 (1.97-3.29)	2.46 (1.79-3.13)	3.31 (2.51-4.12)	2.3 (1.79-2.8)	2.54 (1.88-3.2)
	2100	2.49 (1.84-3.12)	2.37 (1.72-3.03)	2.95 (2.18-3.73)	2.29 (1.79-2.79)	2.38 (1.76-3.02)
<b>SSP2-4.5</b>	2050	2.46 (1.78-3.16)	2.4 (1.73-3.06)	3.14 (2.35-3.97)	2.56 (1.93-3.19)	2.12 (1.45-2.8)
	2070	3.10 (2.34-3.89)	3.01 (2.26-3.76)	4.09 (3.14-5.07)	3.01 (2.38-3.64)	2.72 (1.94-3.5)
	2100	3.66 (3.07-4.27)	3.53 (2.92-4.14)	4.51 (3.85-5.23)	3.59 (3.08-4.09)	3.34 (2.74-3.94)
<b>SSP5-8.5</b>	2050	3.12 (2.55-3.9)	2.84 (2.09-3.58)	4.21 (3.43-5.03)	3.08 (2.56-3.60)	2.99 (2.34-3.64)
	2070	4.61 (4.17-5.28)	4.44 (3.81-5.08)	6.22 (5.55-6.97)	4.27 (3.87-4.68)	4.3 (3.8-4.83)
	2100	7.22 (6.79-8.15)	6.86 (6.05-7.67)	9.87 (9.19-10.6)	6.57 (6.08-7.06)	6.99 (6.31-7.6)

702

## Supplementary Files

This is a list of supplementary files associated with this preprint. Click to download.

- [SupplementaryMaterial.docx](#)